ESC European Society of Cardiology

Cardiovascular Research (2024) **120**, 273–285
https://doi.org/10.1093/cvr/cvad178

Remodelling of cAMP dynamics within the SERCA2a microdomain in heart failure with preserved ejection fraction caused by obesity and type 2 diabetes

Ping Lai[1,2,3], Susanne S. Hille[2,4], Hariharan Subramanian[1,2], Robert Wiegmann[1], Pia Roser[5], Oliver J. Müller [2,4], Viacheslav O. Nikolaev [1,2]*, and Kirstie A. De Jong [1,2]*

[1]Institute of Experimental Cardiovascular Research, University Medical Center Hamburg-Eppendorf, Martinistr. 52, D-20246 Hamburg, Germany; [2]German Center for Cardiovascular Research (DZHK), partner site Hamburg/Kiel/Lübeck, Martinistr. 52, D-20246 Hamburg, Germany; [3]Department of Cardiology, Key Laboratory of Prevention and Treatment of Cardiovascular and Cerebrovascular Diseases, Ministry of Education, First Affiliated Hospital of Gannan Medical University, 341000 Ganzhou, China; [4]Department of Internal Medicine III, University Hospital Schleswig-Holstein, University of Kiel, Arnold-Heller-Str. 3, D-24105, Kiel, Germany; and [5]Department of Endocrinology and Diabetes, University Medical Center Hamburg-Eppendorf, Martinistr. 52, Hamburg D-20246, Germany

Received 19 August 2022; revised 3 August 2023; accepted 23 September 2023; online publish-ahead-of-print 14 December 2023

Time of primary review: 44 days

See the editorial comment for this article 'SERCA2a microdomain cAMP changes in heart failure with preserved ejection fraction', by M. Gotthardt and S.E. Lehnart, https://doi.org/10.1093/cvr/cvae030.

Aims Despite massive efforts, we remain far behind in our attempts to identify effective therapies to treat heart failure with preserved ejection fraction (HFpEF). Diastolic function is critically regulated by sarcoplasmic/endoplasmic reticulum (SR) calcium ATPase 2a (SERCA2a), which forms a functional cardiomyocyte (CM) microdomain where 3′,5′-cyclic adenosine monophosphate (cAMP) produced upon β-adrenergic receptor (β-AR) stimulation leads to phospholamban (PLN) phosphorylation and facilitated Ca^{2+} re-uptake.

Methods and results To visualize real-time cAMP dynamics in the direct vicinity of SERCA2a in healthy and diseased myocytes, we generated a novel mouse model on the $lepr^{db}$ background that stably expresses the Epac1-PLN Förster resonance energy transfer biosensor. Mice homozygous for the leprdb mutation (*db/db*) developed obesity and type 2 diabetes and presented with a HFpEF phenotype, evident by mild left ventricular hypertrophy and elevated left atria filling pressures. Live cell imaging uncovered a substantial β_2-AR subtype stimulated cAMP response within the PLN/SERCA2a microdomain of *db/db* but not healthy control (*db/+*) CMs, which was accompanied by increased PLN phosphorylation and accelerated calcium re-uptake. Importantly, *db/db* CMs also exhibited a desensitization of β_1-AR stimulated cAMP pools within the PLN/SERCA2a microdomain, which was accompanied by a blunted lusitropic effect, suggesting that the increased β_2-AR control is an intrinsic compensatory mechanism to maintain PLN/SERCA2a-mediated calcium dynamics and cardiac relaxation. Mechanistically, this was due to a local loss of cAMP-degrading phosphodiesterase 4 associated specifically with the PLN/SERCA2a complex.

Conclusion These newly identified alterations of cAMP dynamics at the subcellular level in HFpEF should provide mechanistic understanding of microdomain remodelling and pave the way towards new therapies.

* Corresponding authors. Tel: +0049 40 7410 57095; fax: +0049 40 7410 40180; E-mail: v.nikolaev@uke.de (V.O.N.); k.dejong.ext@uke.de (K.A.D.J.)

Graphical Abstract

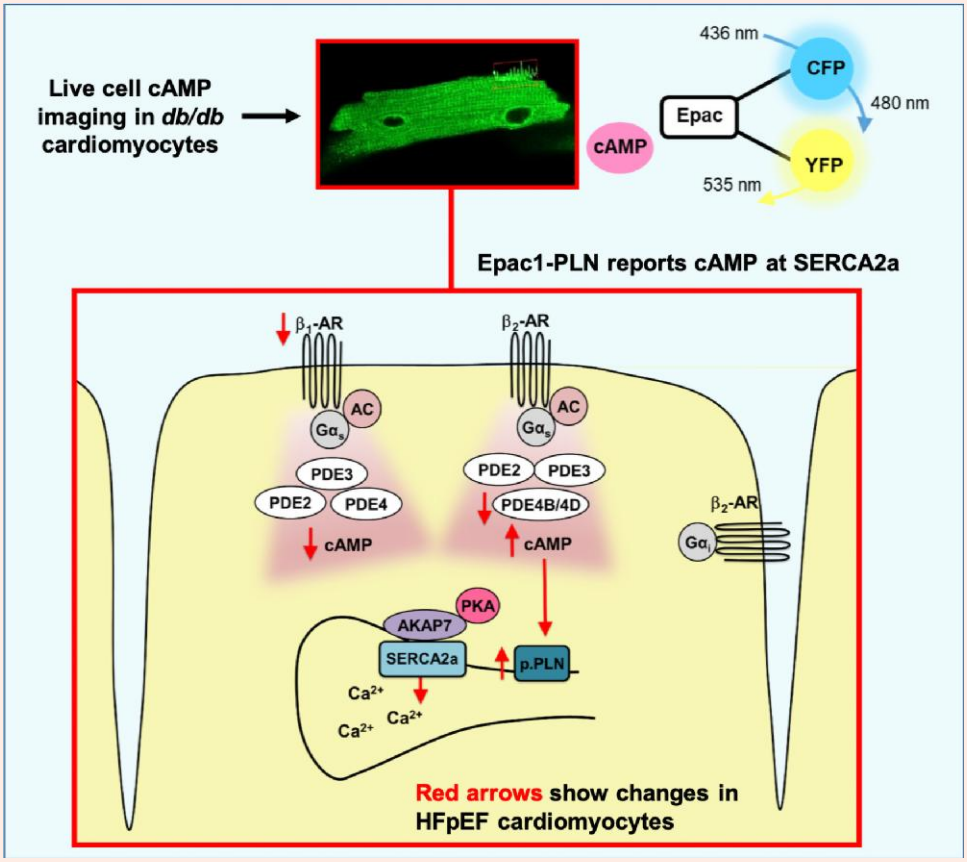

Keywords Heart failure with preserved ejection fraction • Obesity • Type 2 diabetes • Phospholamban • Sarcoplasmic/endoplasmic reticulum calcium ATPase 2a • 3′, 5′-Cyclic adenosine monophosphate • Phosphodiesterase • Förster resonance energy transfer

1. Introduction

Heart failure with preserved ejection fraction (HFpEF) is on track to become the most prominent form of heart failure, with its incidence soon set to take over that of traditional heart failure with reduced ejection fraction (HFrEF). Of major concern is that we currently lack effective therapies to treat HFpEF,[1] which is perhaps not surprising considering the many aetiologies and broad nature of HFpEF diagnosis that we are just in the early stages of understanding. Obesity and type 2 diabetes (T2D) are arguably the most prominent causes of HFpEF, independent of pressure overload stresses and age.[2–4] Given the increasing prevalence of obesity and T2D worldwide,[5] we are in urgent need of a greater understanding of the pathophysiology of obesity and T2D-induced HFpEF. In the current study, we propose the foundation for this understanding lies in the investigation of 3′,5′-cyclic adenosine monophosphate (cAMP) dynamics within the sarcoplasmic/endoplasmic reticulum (SR) calcium ATPase 2a (SERCA2a) microdomain, an integral site of cardiomyocyte (CM) relaxation.

cAMP is produced via β-adrenergic receptor (β-AR) signalling and inhibited via AMP-hydrolyzing enzyme phosphodiesterases (PDEs), for which there are at least five families expressed in the heart (PDE1, 2, 3, 4, and 8).[6] Increases in cAMP result in the activation of cAMP-dependent protein kinase (PKA) and exchange protein directly activated by cAMP (Epac), proteins which influence calcium influx and re-uptake by activating calcium-handling proteins such as the L-type calcium channels (LTCCs), ryanodine receptors (RyRs), and SERCA2a.[7] These calcium-handling proteins are thought to centre distinct microdomains within the cell, in which cAMP activity is regulated via the spatial organization of different β-AR subtypes, protein kinases tethered to specific A-kinase anchoring proteins (AKAPs), and PDEs.[8] In recent years, the generation of cAMP biosensors targeted to these calcium-handling proteins has allowed high spatial and temporal resolution of cAMP dynamics within these microdomains, resulting in unprecedented advances in our understanding of cAMP microdomain remodelling in the pathophysiology of disease, especially in HFrEF.[9–11] Unfortunately, in obesity and T2D HFpEF (let alone in any aetiology of HFpEF), our understanding of cAMP dynamics both at the whole cell level and microdomain level lags considerably behind that of HFrEF.[12] This is the first study to our knowledge that attempts to resolve cAMP dynamics at the microdomain level in HFpEF.

In this work, we generated a novel mouse model on the lepr^{db} background that stably expresses the targeted Epac1-phospholamban (PLN) biosensor based on Förster resonance energy transfer (FRET).[9] Epac1-PLN is comprised of the highly sensitive cAMP biosensor Epac1-camps fused to PLN, a regulatory protein of SERCA2a, which associates with and inhibits SERCA2a activity. This inhibition is relieved by PKA-dependent PLN phosphorylation, occurring upon β-AR stimulation and cAMP production. Diastolic dysfunction linked to alterations in PLN/

SERCA2a ratios and in PLN phosphorylation/SERCA2a activity has been reported in the human T2D heart and in a wide array of obese/T2D mouse models,[13–16] yet the intricate mechanisms leading to these alterations remain unclear.

In the current study, we have employed the lepr^{db} mouse model as our model of obesity and T2D-induced HFpEF. These mice harbour a recessive mutation in their leptin receptor; leptin is a hormone that regulates appetite and energy expenditure.[17] Mice homozygous for this mutation have a dysfunctional leptin receptor, and as such, they overeat and develop obesity and insulin resistance by 3–4 weeks of age, which progresses to T2D by the age of 8–10 weeks.[18,19] We have previously shown that at 16 weeks of age, these mice exhibit a HFpEF phenotype with the presence of diastolic dysfunction and preserved systolic function. While it is difficult to identify a mouse model that can completely recapitulate the complex nature of obesity and T2D HFpEF, this model was chosen instead of other obesity and T2D HFpEF mouse models such as high-fat diet and streptozocin induced, as high-fat diets often induce a pre-T2D phenotype and are complicated by the additional variable of an exogenous fat supply, and the streptozocin model is more representative of type 1 diabetes and/or late-stage insulin-deficient T2D and is not driven by insulin resistance but by the ablation of beta-cells and ability to produce enough insulin. In contrast, *db/db* mice exhibit a T2D pathophysiology that is comparable to that in humans, developing obesity, hyperinsulinaemia, and insulin resistance that progresses to T2D, which is not complicated by the presence of an exogenous supply of fats from a high-fat diet or hypertension.

With the use of the Epac1-PLN biosensor, we were able to visualize cAMP dynamics in direct vicinity of SERCA2a to gain answers into the mechanisms of cAMP remodelling that promote altered PLN/SERCA2a activity in HFpEF caused by obesity and T2D. In particular, we uncovered that HFpEF leads to β_2-AR-dependent increases of local cAMP, PLN phosphorylation, and acceleration of calcium re-uptake into the SR.

2. Methods

2.1 Generation of lepr^{db} mouse line expressing PLN-Epac1 biosensor

To generate the obese and T2D mouse line stably expressing the Epac1-PLN biosensor in the heart, mice heterozygous for the lepr^{db} mutation were bred with mice expressing the Epac1-PLN biosensor driven by the α-MHC promoter. As the previously described[9] Epac1-PLN mice were on the FVB/N background, both the lepr^{db} and Epac1-PLN mice were back crossed to the C57BL/6N background. Mice heterozygous for both lepr^{db} and Epac1-PLN were then bred to generate experimental animals. Heterozygous lepr^{db} mice (*db*/+) harboured a functional leptin receptor and were healthy lean controls in the study, and mice homozygous for lepr^{db} (*db/db*) harboured a dysfunctional leptin receptor and were the obese and T2D mice in the study. Genotyping of the lepr^{db} was performed via standard polymerase chain reaction (PCR) using the primers 5′-AGAA CGGACACTCTTTGAAGTCTC-3′ and 5′-TGA TGC CCT GAA AAT CAA GC-3′ followed by a restriction digest with Hpy166. Genotyping of the Epac1-PLN was performed using the primers 5′-TGACAGACAGA TCCCTCCTAT-3′ and 5′-CATGGCGGACTTGAAGAAGT-3′. Mouse breeding and experiments were performed in accordance with ARRIVE guidelines and following institutional and governmental guidelines of the BJV Hamburg (approval numbers N106/2020 and N019/2018) and the Directive 2010/63/EU of the European Parliament.

2.2 Echocardiography

Sixteen-week-old mice were anesthetized with 1.5–2% isoflurane to maintain a heart rate between 400 and 500 b.p.m. Echocardiography was performed using the Vevo 3100 and MX550D (40 MHz) transducer in which left ventricular structural measurements were obtained in the short-axis view using 2D B-mode and M-mode images including left ventricular internal diameter during diastole and systole (LVIDd, LVIDs), interventricular septum diameter during diastole and systole (IVSd, IVSs),and left ventricular posterior wall diameter during diastole and systole (LVPWd, LVPWs). Left ventricular structural measurements were used to obtain systolic indices, ejection fraction (EF), and fractional shortening (FS). Diastolic function was assessed in the four chambers view via pulsed-wave Doppler and tissue Doppler including peak E-wave, E′, peak A-wave, isovolumic relaxation time (IVRT), and deceleration time (DT). Left atria (LA) size was obtained in long-axis view in M-mode. All echocardiographic data were analysed using Vevo Lab software.

2.3 Adult ventricular CM isolation

Adult ventricular CMs were isolated via Langendorff perfusion. Mice were euthanized with 3–4% isoflurane followed by cervical dislocation, and the hearts were excised and transferred to ice-cold phosphate buffered saline (PBS) where the aorta was cannulated to a custom 21G cannula. The heart was then perfused at 37°C with perfusion buffer (in mM: NaCl 113, KCl 4.7, KH_2PO_4 0.6, $Na_2HPO_4 \times 2H_2O$ 0.6, $MgSO_4 \times 7H_2O$ 1.2, $NaHCO_3$ 12, $KHCO_3$ 10, HEPES 10, taurine 30, 2,3-butanedione monoxime 10, and glucose 5.5, pH 7.4), followed by further perfusion with a digestion buffer containing an additional collagenase (NB-70 S1747403; Nordmark Pharma), trypsin (0.025%, Gibco), and $CaCl_2$ 12.5 mM. The ventricular tissue was then removed and cut into small pieces in digestion buffer, after which an equal volume of perfusion buffer containing 1% bovine serum albumin (BSA) and 50 μM $CaCl_2$ was added to inactivate the digestive enzymes. The tissue was then titrated to release the cells, which were passed through a filter before sedimentation. The CM pellet was re-suspended in perfusion buffer containing 0.5% BSA and 37.5 μM $CaCl_2$ and underwent gradual re-calcification up to a final concentration of 1 μM calcium. The CMs were plated onto laminin-coated coverslips (25 mm, Thermo Fisher Scientific) and incubated at 37°C and 5% CO_2 for later FRET measurements. In the case of protein/immunoblot analysis, the CM pellet was re-suspended without BSA.

2.4 Immunoblots and co-immunoprecipitation

CMs were homogenized in ice-cold RIPA buffer (50 mM Tris pH 7.5, 0.1 M NaCl, 0.1% SDS, 1% NP-40, 1 mM EGTA, 1% Triton X-100, 0.05% sodium deoxycholate, phosphatase, and protease inhibitor cocktails), and protein concentrations were assessed via standard BC assay. A total of 20–30 μg of protein was separated by SDS-PAGE and transferred onto PVDF membrane using standard protocols. Membranes were blotted for total PLN (Abcam, 124174), phosphorylation Ser16 PLN (Badrilla, A010-12), SERCA2a (Enzo, ALX-804-088-RI00), RYR (Sigma, B118272), AKAP7 (Proteintech, 12591-1-AP), PKA RIIα subunit (BD Bioscience, 612242), PDE2A (Fabgennix, PPD2A-101AP), PDE3A (kind gift from Chen Yan), PDE4B (Abcam, ab170939), PDE4D (Abcam, ab171750), and calsequestrin (Thermo Fisher Scientific, PA1-913S). For co-immunoprecipitation (Co-IP) experiments, 800 μg of protein lysate was incubated with total PLN antibody for 8 h at 4°C, followed by an overnight incubation with the beads that were then washed and subjected to either immunoblot analysis or calorimetric PDE activity assay (Abcam, ab241034) according to manufacturer instructions. For subcellular fractionation, heart lysates were applied to sucrose gradient to isolate plasma membrane and sarcolemmal CM fractions exactly as previously described.[11]

2.5 FRET measurements and data analysis

Laminin-coated cover slides with isolated CMs were transferred into a custom-made chamber. The FRET measurements were then performed as previously described; briefly, FRET buffer (in mM: 144 NaCl, 5.4 KCl, 1 $MgCl_2$, 1 $CaCl_2$, and 10 HEPES, pH 7.3) was added to the chamber containing the cells, and the FRET measurements were taken using an inverted fluorescent microscope (Nikon Ti) and MicroManager 1.4 software. A CoolLED 440 nm light source was used to excite the donor fluorophore, cyan fluoresce protein (CFP), using a filter cube containing 436 ± 30 nm excitation filter and DCLP455 dichroic mirror. Emitted light from the acceptor fluorophore was split into CFP and yellow florescent protein

(YFP) channels using DV2 DualView (Photometrics). Images from the CFP and YFP emission channels were acquired every 10 s. The ratio of the emitted lights from CFP and YFP was measured offline using ImageJ software and copy pasted into an Excel spreadsheet to calculate the corrected FRET ratio.

2.6 IonOptix experiments

CMs plated onto laminin-coated dishes were incubated for 20 min in Fura-2 AM, 2 μM (Thermo Fisher Scientific, 2286856), diluted in IonOptix buffer (in mM: 135 NaCl, 4.7 KCl, 0.6 KH_2KPO_4, $0.6Na_2HPO_4 \times 2H_2O$, 1.2 $MgSO_4 \times 7H_2O$, 1.5 $CaCl_2$, 20 glucose, and 10 HEPES, pH 7.4). Fura-2 AM was washed out, and CMs were incubated for a further 30 min in IonOptix buffer prior to the start of measurements. CMs were paced at 1 Hz field stimulation using MyoPacer field stimulator (20 V, 4 ms). Ca^{2+} transients were recorded (over 15–20 stable contractions, excitation at 360/380 nm, and emission at 510 nm), and data were analysed by the transient analysis tool software.

2.7 Statistics

Data were analysed using the Origin Pro 8.5 (OriginLab Corporation, Northampton, MA), Prism 7 (GraphPad, San Diego, CA), and R 3.6.3 software (R Foundation for Statistical Computing, Vienna, Austria). Data were assessed for normal distribution by Kolmogorov–Smirnov test, and for data with $n < 6$, normality was tested with Shapiro–Wilk test. Comparisons between normally distributed data were analysed by nested analysis of variance (ANOVA), mixed ANOVA followed by Wald χ^2 test, one-way ANOVA followed by Sidak multiple comparisons test, and paired or unpaired *t*-test for comparisons between two groups. Groups of unpaired nonparametric data were analysed by Mann–Whitney test or by Kruskal–Wallis ANOVA followed by Dunn's multiple comparisons test. $^*P < 0.05$ was considered significant. All data are shown as mean ± SEM, unless otherwise specified.

Table 1 Basic characteristics and transthoracic echocardiography

Variable	*db/+*	*db/db*	*P* value
Weight (g)	31.47 ± 4.90	54.89 ± 9.07***	<0.001
Blood glucose (mg/dL)	138 ± 26.89	444 ± 131.7***	<0.001
Heart rate (b.p.m.)	409 ± 50	419 ± 54	0.6833
IVSd (mm)	0.82 ± 0.23	0.93 ± 0.13*	0.0330
IVSs (mm)	1.25 ± 0.40	1.46 ± 0.24**	0.0780
LVIDd (mm)	4.12 ± 0.66	3.91 ± 0.51	0.4285
LVIDs (mm)	2.83 ± 0.88	2.54 ± 0.51	0.1645
LVPWd (mm)	0.67 ± 0.14	0.88 ± 0.12**	0.0307
LVPWs (mm)	1.07 ± 0.34	1.21 ± 0.16	0.1564
Estimated LV mass (mg)	96.1 ± 10.6	127.2 ± 35.6**	0.0191
LA (mm)	1.03 ± 0.09	1.38 ± 0.27*	0.0342
EF (%)	59.7 ± 17.6	62.1 ± 9.4	0.6801
FS (%)	33.1 ± 17.8	33.2 ± 7.0	0.2775
Peak E-wave	716 ± 147	736 ± 88	0.7217
Peak A-wave	421 ± 49	403 ± 142	0.7255
E/A	1.92 ± 0.26	1.67 ± 0.55	0.3890
IVRT (ms)	14.39 ± 3.88	17.78 ± 1.61*	0.0224
e′	25.34 ± 6.06	16.11 ± 4.16***	<0.001
E/e′	28.98 ± 8.93	49.87 ± 11.95*	0.1520

Data presented as mean ± SD.
IVSd, interventricular septum diameter during diastole; IVSs, interventricular septum diameter during systole; LVIDd, left ventricular internal diameter during diastole; LVIDs, left ventricular internal diameter during systole; LVPWd, left ventricular posterior wall diameter during diastole; LVPWs, left ventricular posterior wall diameter during systole; LA, left atria; EF, ejection fraction; FS, fractional shortening; IVRT, isovolumic relaxation time; DT, deceleration time. $^*P < 0.05$, $^{**}P < 0.01$ and $^{***}P < 0.001$ compared to db/+ controls.

3. Results

3.1 *db/db* mice exhibit a HFpEF phenotype

At 16 weeks of age, body weight and blood glucose were increased in *db/db* mice compared to *db/+* (31.5 vs. 54.9 g and 138 vs. 444 mg/dL, respectively, *Table 1*). Transthoracic echocardiography analysis was performed to assess cardiac structure and function in the mice, with *db/db* mice found to exhibit mild left ventricular hypertrophy, evident by increased IVSd, LVPWd, and LV mass (*Figure 1A*, *B*, and *G* and *Table 1*) and CM cell size, as confirmed by wheat germ agglutinin (WGA) staining (see Supplementary material online, *Figure S1A and B*). This was accompanied by severe diastolic dysfunction as observed by an increased IVRT and preserved mitral valve velocity (peak E-wave) accompanied by reduced tissue movement (e′) during early relaxation (characteristic of pseudonormal filling). Furthermore, an increased E/e′ ratio and LA dimension in *db/db* mice indicate increased LA filling pressure, a defining feature of HFpEF (*Figure 1D–F*, *H*, and *I* and *Table 1*). Accompanying this diastolic dysfunction, *db/db* hearts exhibited increased picrosirius red staining (approximately two-fold increase) and increased CM mRNA expression of *Col1a1* (*Figure 1J–L*), indicating the presence of LV fibrosis. Importantly, systolic function was preserved in *the db/db* mice, consistent with the presence of HFpEF (*Figure 1C* and *G* and *Table 1*).

3.2 *db/db* CMs exhibit altered β-AR stimulation of PLN phosphorylation, despite no changes in the expression levels of cAMP regulatory proteins at the whole cell level

To gain a snapshot of β-AR signalling in the mice, CMs were isolated and the protein expression of PDEs and essential calcium-handling proteins was assessed. No changes in PDE2A, PDE3A, PDE4B, or PDE4D were observed, nor in total protein levels of RyR, SERCA2a, or cTnI (*Figure 1M* and *N*). However, *db/db* mice exhibited a trend for increased total PLN and for decreased SERCA2a levels ($P = 0.06$) with the PLN/SERCA2a ratio significantly elevated in *db/db* hearts (*Figure 1N* and *O*), compatible with published data for this HFpEF model.[16] Considering phosphorylation of PLN, basal phosphorylation levels at Ser16 were unchanged between the groups, and upon selective β_1-AR stimulation, significant increases in Ser16 phosphorylation were observed at both submaximal (ICI118551 50 nM + ISO 3 nM) and maximal (ICI118551 50 nM + ISO 100 nM) stimulation in both *db/+* and *db/db* CMs, suggesting preserved β_1-AR-mediated regulation of PLN phosphorylation in *db/db* CMs (*Figure 1P* and *Q*). As expected, selective β_2-AR stimulation (CGP20712A 100 nM + ISO 100 nM) failed to increase Ser16 phosphorylation in *db/+* CMs but interestingly resulted in significant increases in Ser16 phosphorylation in *db/db* CMs (~7.5-fold greater in *db/db* CMs, $P < 0.05$, *Figure 1P* and *Q*), suggesting the presence of altered β-AR control and/or cAMP dynamics that favour increased β_2-AR signalling within the PLN/SERCA2a microdomain in *db/db* CMs. To explore this further, we assessed cAMP dynamics in real time in living isolated CMs from *db/+* and *db/db* mice stably expressing the Epac1-PLN biosensor.

3.3 *db/db* CMs exhibit increased β_2-AR-stimulated cAMP pools within the PLN/SERCA2a microdomain accompanied by enhanced PLN phosphorylation and accelerated calcium re-uptake

Both *db/+* and *db/db* CMs from mice stably expressing the Epac1-PLN biosensor exhibited co-localization of the PLN-Epac1 biosensor with SERCA2a, as confirmed by confocal imaging (see Supplementary material

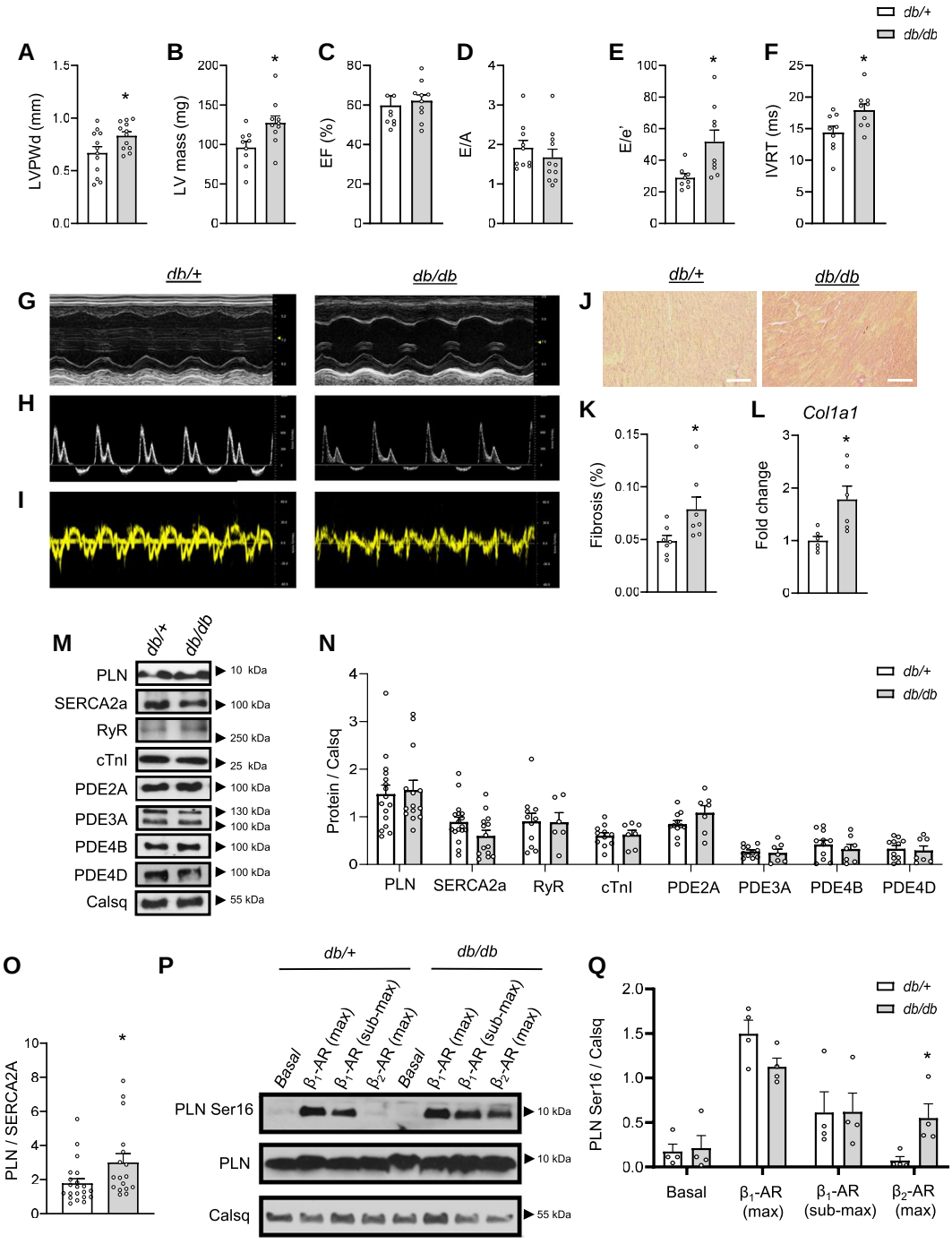

Figure 1 HFpEF phenotype and 'snapshot' of β-AR subtype signalling. (*A*) Left ventricular posterior wall during diastole (LVPWd), (*B*) left ventricle mass (LV mass), (*C*) ejection fraction % (EF %), (*D*) E/A ratio, (*E*) E/e', and (*F*) isovolumic relaxation time (IVRT). Representative transthoracic echocardiography images, (*G*) short-axis view of the left ventricle in M-mode, (*H*) pulsed-waved Doppler, and (*I*) tissue Doppler from four-chamber view. (*J*) Representative images of picrosirius red, scale bar 40 µm, and (*K*) quantification ($N = 5$ mice/group). (*L*) Fold change in *Col1a1* mRNA expression ($N = 6$ mice/group). (*M*) Representative images and (*N*) quantification of the protein expression of total PLN, SERCA2a, RyR, cTnI, PDE2A, PDE3A, PDE4B, and PDE4D, normalized to calsequestrin (Calsq; $N = 6$–15 hearts/group). (*O*) Quantification of the PLN/SERCA2a ratio from the data shown in (*N*). (*P*) Representative blots and (*Q*) quantification of Ser16 PLN phosphorylation at both submaximal (3 nM ISO + 50 nM ICI118551) and maximal (100 nM ISO + 50 nM ICI118551) selective β_1-AR stimulation and of maximal selective β_2-AR stimulation (100 nM ISO + 100 nM CGP20712A; $N = 4$ mice/group). Normal distribution in (*A–F*, *K*, *L*, *N*, and O) was confirmed by Kolmogorov–Smirnov test ($P > 0.1$); in (*Q*), normal distribution was tested by Shapiro–Wilk test, *P* values were $P = 0.0777$, $P = 0.6468$, $P = 0.0357$, $P = 0.0069$, $P = 0.0447$, $P = 0.4695$, $P = 0.1930$, and $P = 0.0594$, respectively. Significance at $^*P < 0.05$. Normally distributed data in (*A–F*, *K*, *L*, and *O*) analysed by unpaired *t*-test and in (*N*) by mixed ANOVA followed by Wald χ^2 test and Sidak multiple comparisons test for data not normally distributed; (*Q*) analysis performed by Kruskal–Wallis ANOVA followed by Dunn's multiple comparison test. $^*P < 0.05$ vs. *db/+* same condition.

online, *Figure S2A*). In our first FRET experiments, we aimed to determine the level of cAMP FRET response that could be induced in the CMs with selective β-AR subtype stimulation and to study whether β-AR sensitivity is maintained and/or whether there is any remodelling of β-AR subtype control of cAMP dynamics within the SERCA2a microdomain in obesity/T2D HFpEF. To identify the appropriate concentration of our nonselective β-AR agonist ISO to perform these experiments, we measured concentration response dependencies identifying 1 and 100 nM ISO to be the lowest concentrations of ISO to induce submaximal (~50%) and saturating cAMP FRET responses, respectively, in both *db/+* and *db/db* CMs (see Supplementary material online, *Figure S2B*). To determine which β-AR subtype is responsible for producing cAMP pools within the PLN/SERCA2a microdomain, we stimulated the CMs with ISO in the presence of either the β_1-AR (CGP20712A) or the β_2-AR (ICI118551) antagonist and compared the percentage change in FRET to the maximum cAMP level that could be achieved by subsequent treatment with the pan-PDE inhibitor IBMX (100 μM) and an adenylyl cyclase activator forskolin (10 μM), thus allowing us to bypass the β-ARs to induce a maximal cAMP response and/or biosensor saturation. Selective β_1-AR stimulation at submaximal concentrations (1 nM ISO + 50 nM ICI118551) induced a somewhat blunted increase in the FRET response in *db/db* CMs compared to *db/+* at 33% vs. 40% of max, respectively, while maximal stimulation (100 nM ISO + 50 nM ICI118551) induced a comparable percentage change in the FRET response in both *db/+* and *db/db* CMs at 62 and 58% of max, respectively (*Figure 2A–F*). NanoString nCounter mRNA analysis identified *Ardb1* gene expression to be reduced in *db/db* CMs by 50%, supporting reduced capacity for β_1-AR stimulation at submaximal agonist concentrations (see Supplementary material online, *Figure S3A*). In contrast and in line with Ser16 phosphorylation experiments, selective β_2-AR stimulation induced a significantly higher cAMP FRET amplitude in *db/db* CMs compared to that in *db/+*, with a 55% response to max in *db/db* CMs vs. a 13% response in *db/+* CMs (*Figure 2G–I*). These results were not sex specific, as when separated by sex, both male and female CMs showed the same reduction of submaximal β_1-AR-induced cAMP FRET responses and increased β_2-AR-induced cAMP FRET responses (see Supplementary material online, *Figure S4A and B*). Importantly, no differences in these cAMP FRET measurements were observed in CMs isolated from young mice aged 6 weeks of age, prior to the onset of diastolic dysfunction (see Supplementary material online, *Figure S4D–H*). Interestingly, the increased β_2-AR cAMP FRET responses observed in adult CMs were not accompanied by an increase in *Ardb2* gene expression (see Supplementary material online, *Figure S3B*), suggesting the alterations in cAMP regulation may be occurring downstream of the β_2-AR. Supporting this, when we expressed the Epac1-camp biosensor in the cytosol of the CMs (confirming proper Epac1-camp localization within the cytosol using confocal imaging; Supplementary material online, *Figure S5A*), submaximal and maximal β_1-AR stimulation as well as maximal β_2-AR stimulation resulted in comparable increases in cAMP amplitudes in both *db/+* and *db/db* CMs (see Supplementary material online, *Figure S5B–H*), suggesting the presence of PLN/SERCA2a microdomain-specific β-AR dysregulation. To translate these FRET findings on a functional level, single-cell contractility measurements using IonOptix were performed, in which calcium re-uptake into the SR and sarcomere relaxation upon selective β_1-AR and β_2-AR stimulation were assessed.

Consistent with FRET results, selective β_1-AR stimulation at submaximal concentrations (ISO 0.3 nM + ICI118551 50 nM) resulted in a blunted increase in time to 90% (T_{90}) calcium re-uptake and sarcomere relaxation in *db/db* CMs compared to that in *db/+* CMs (*Figure 2J–L*; Supplementary material online, *Figure S6A*), with these effects masked at higher ISO concentrations (ISO 1 nM + ICI118551 50 nM; *Figure 2M–O*). However, upon selective β_2-AR stimulation (CGP20712A 50 nM + ISO 70 nM), T_{90} calcium re-uptake and sarcomere relaxation were significantly enhanced in *db/db* CMs, while β_2-AR stimulation failed to accelerate calcium re-uptake and relaxation in *db/+* CMs (*Figure 2P–R*; Supplementary material online, *Figure S6A*). This suggests that *db/db* CMs exhibit a desensitization of β_1-AR-induced cAMP levels and lusitropic effects and a shift for β_2-AR control of the PLN/SERCA2a microdomain and of CM relaxation that is not present in *db/+* CMs. As a control experiment, Epac1-PLN-expressing cells also exhibited normal calcium kinetics, with T_{90} calcium re-uptake and peak amplitudes comparable in isolated CMs from mice with and without the Epac1-PLN biosensor (see Supplementary material online, *Figure S6B and C*). Previously, no differences in β-AR stimulation of Ser16 PLN phosphorylation were detected in mice with and without the biosensor supporting the presence of maintained PLN/SERCA2a function in Epac1-PLN-expressing mice.[9]

Of note here, we have previously shown that *db/db* mice exhibit an increased susceptibility to ventricular arrhythmias,[20] and indeed, in our current study, selective β_1-AR stimulation increased arrhythmia occurrence in *db/db* CMs but not *db/+* CMs (see Supplementary material online, *Figure S7A*). However, importantly, the increased β_2-AR-induced cAMP amplitudes, SR calcium re-uptake, and associated calcium load in *db/db* CMs were not accompanied by an increased occurrence of arrhythmic events (see Supplementary material online, *Figure S7B*), suggesting the accelerated calcium re-uptake with β_2-AR stimulation in the *db/db* CMs is not pro-arrhythmic, supporting a possibly beneficial action of increased β_2-AR signalling.

3.4 *db/db* CMs exhibit a decreased coupling of the β_2-AR with PDE4 within the SERCA2a microdomain

To look more closely at the mechanisms that may be inducing increased β_2-AR-stimulated cAMP pools within the PLN/SERCA2a microdomain, coupled PDE responses were assessed via FRET. In order to prevent biosensor saturation, submaximal β-AR stimulation was used in these FRET experiments where the β_1-AR (ISO 1 nM + ICI118551 50 nM) and β_2-AR (ISO 1 nM + CGP20712A 100 nM) were selectively stimulated, after which individual PDEs were inhibited by treatment with inhibitors for PDE2, PDE3, or PDE4, followed by treatment with IBMX (100 μM) to identify the percentage contribution of each PDE family to that of total PDE inhibition. Interestingly, despite *db/db* CMs exhibiting reduced cAMP amplitudes in response to submaximal β_1-AR stimulation, no changes in FRET responses were observed with inhibition of PDE2 [100 nM BAY 60-7550, (Bay)], PDE3 [10 μM cilostamide (Cilo)], or PDE4 [10 μM rolipram (Roli)] following submaximal selective β_1-AR stimulation (*Figure 3A–F* and *M*) suggesting the decreased β_1-AR-induced cAMP pools within the PLN/SERCA2a microdomain were not a result of increased coupled PDE activity and cAMP hydrolysis. Considering selective β_2-AR stimulation, inhibition of PDE4 resulted in a blunted increase in FRET amplitudes in *db/db* CMs compared to that in *db/+* with a 37% change in FRET compared to IBMX in *db/db* vs. 54% in *db/+*, while inhibition of PDE2 and PDE3 post selective β_2-AR stimulation resulted in comparable increases in FRET (*Figure 3G–L* and *N*). This blunted effect of PDE4 inhibition was comparable in female and male CMs (see Supplementary material online, *Figure S4C*). Interestingly, when basal PDE activities were assessed, basal Roli treatment resulted in an increased percentage change in FRET and PLN Ser16 phosphorylation in *db/db* CMs compared to that in *db/+* CMs (see Supplementary material online, *Figure S8A–E*), which may explain the maintained basal PLN Ser16 phosphorylation levels observed, despite the presence of prolonged basal calcium re-uptake in the *db/db* CMs. Importantly, basal PDE inhibition will occur globally throughout the cell, and this is contrast to PDE inhibition post β-AR stimulation, in which the effects of PDE inhibition are more strongly compartmentalized; therefore, it is difficult to accurately assess basal PDE activities within distinct microdomains.

We looked more closely at these FRET findings where we observed a loss of PDE4 coupled to the β_2-AR, by investigating the functional effects of PDE4-mediated regulation of β_2-AR-induced calcium re-uptake. In *db/+* CMs, PDE4 inhibition with Roli post selective β_2-AR stimulation unmasked a β_2-AR-induced acceleration of calcium re-uptake; however, in *db/db* CMs, additional treatment with Roli had no effect on calcium re-uptake post β_2-AR stimulation (*Figure 4A*; Supplementary material online, *Figure S6D and E*), whereas subsequent effect of IBMX was comparable

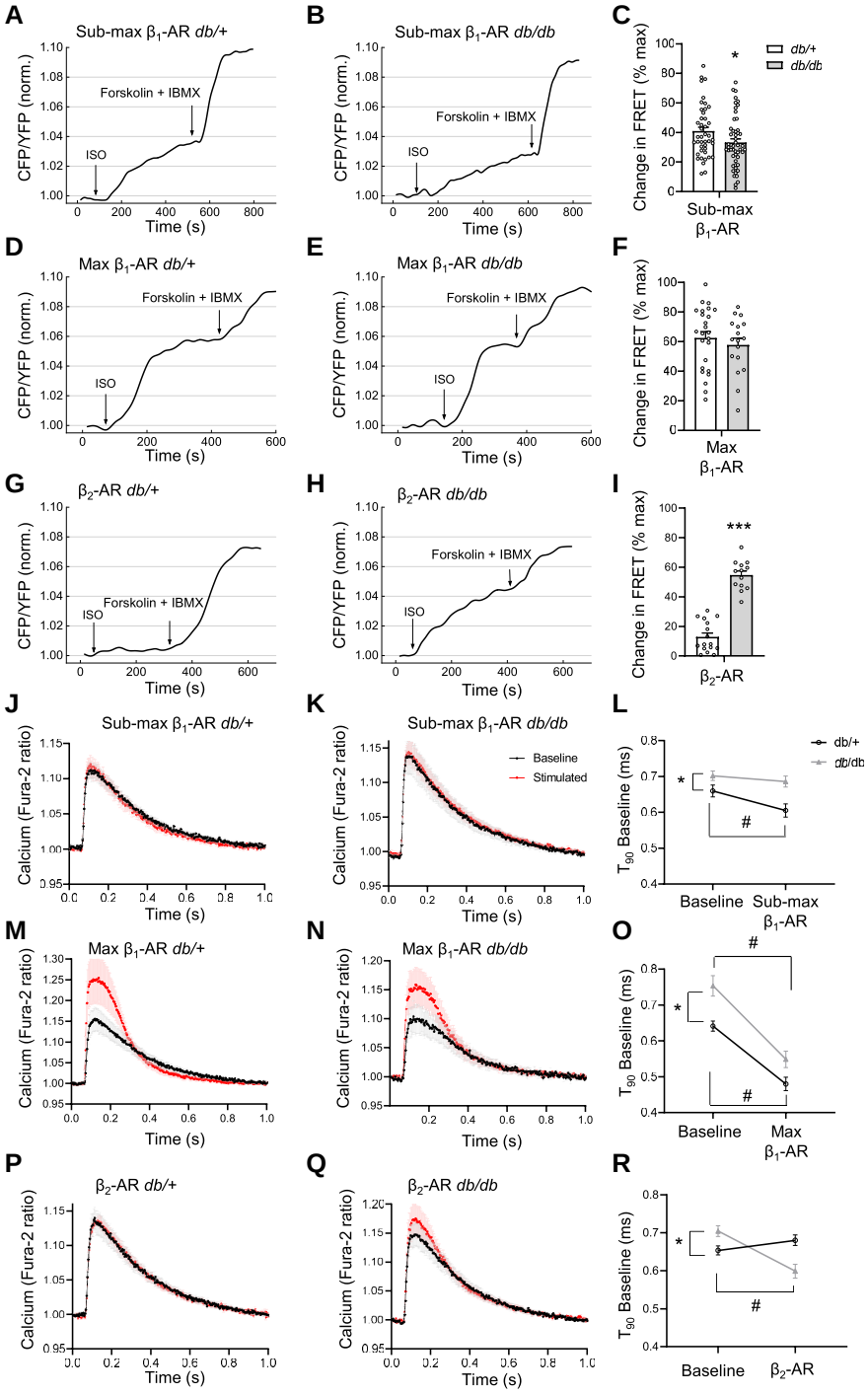

Figure 2 Real-time monitoring of cAMP levels in the SERCA2a microdomain post selective β-adrenergic stimulation. Representative cAMP FRET traces obtained from selective β-AR stimulation in *db/+* and *db/db* CMs, as well as quantification of the % change in FRET as compared to maximum response induced by 10 μM forskolin and 100 μM IBMX. Representative traces for submaximal β_1-AR stimulation (1 nM ISO in the presence of 50 nM ICI118551) in (*A*) *db/+* ($N = 17$ mice/45 cells) and (*B*) *db/db* CMs ($N = 15$ mice/32 cells) quantified in (*C*), for maximal β_1-AR stimulation (100 nM ISO in the presence of 50 nM ICI118551) in (*D*) *db/+* ($N = 8$ mice/26 cells) and (*E*) *db/db* ($N = 5$ mice/17 cells) CMs quantified in (*F*), and for β_2-AR stimulation (100 nM ISO in the presence of 100 nM CGP20712A) in (*G*) *db/+* ($N = 10$ mice/17 cells) and (*H*) *db/db* ($N = 4$ mice/13 cells) CMs quantified in (*I*). T_{90} calcium re-uptake with submaximal β_1-AR stimulation (0.3 nM ISO + 50 nM ICI118551) in (*J*) *db/+* ($N = 3$ mice/61 cells) and (*K*) *db/db* ($N = 3$ mice/69 cells) CMs and (*L*) quantification, with maximal β_1-AR stimulation (1 nM ISO + 50 nM ICI118551) in (*M*) *db/+* ($N = 4$ mice/62 cells) and (*N*) *db/db* ($N = 3$ mice/29 cells) CMs and (*O*) quantification, and for β_2-AR stimulation (70 nM ISO + 100 nM CGP20712A) in (*P*) *db/+* ($N = 4$ mice/72 cells) and (*Q*) *db/db* ($N = 4$ mice/56 cells) CMs and (*R*) quantification. Normal distribution was tested by Kolmogorov–Smirnov test ($P > 0.1$) in all data except (*C*) where *db/+*, $P = 0.0771$ and *db/db*, $P = 0.0448$ and (*I*) where *db/+*, $P = 0.0132$. Data in (*C*, *F*, and *I*) were then analysed by Kruskal–Wallis ANOVA followed by Dunn's multiple comparison test. For data in (*L*, *O*, and *R*), comparisons of baseline and stimulated within the same group were analysed by paired *t*-test, and comparisons of baselines and stimulated between different groups were analysed by unpaired *t*-test. $*P < 0.05$ and $***P < 0.001$ vs. *db/+* same condition. $\#P < 0.05$ vs. baseline same group.

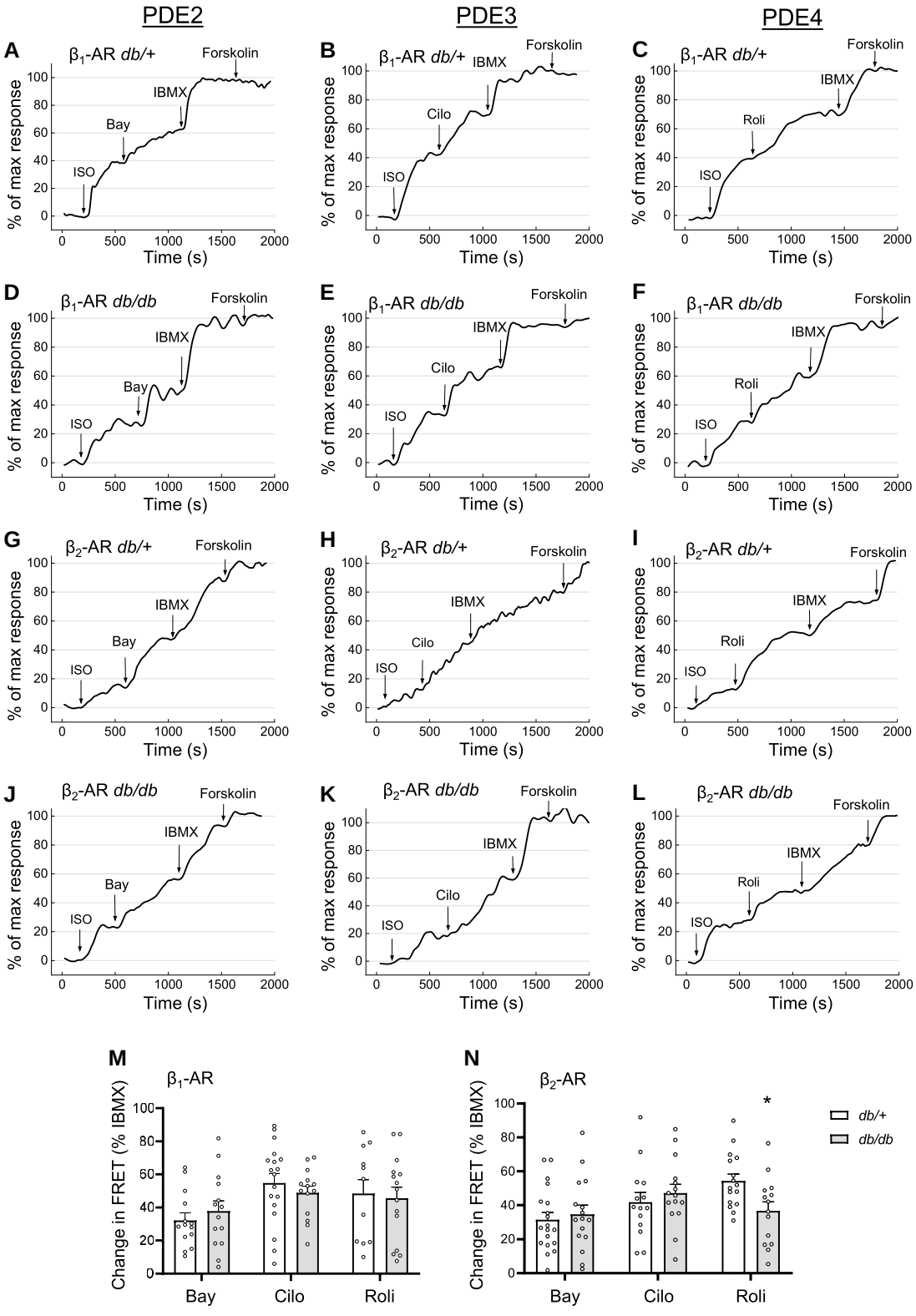

Figure 3 Role of PDEs in cAMP regulation after selective β-AR subtype stimulations. Representative cAMP FRET traces of selective PDE2 (100 nM BAY 60-7550, Bay), PDE3 (10 μM Cilo), and PDE4 inhibition (10 μM Roli) inhibition post selective β_1-AR (100 nM ISO in the presence of 50 nM ICI118551) stimulation in (*A–C*) *db/+* (Bay, $N = 4$ mice/12 cells; Cilo, $N = 7$ mice/16 cells; Roli, $N = 7$ mice/13 cells) and (*D–F*) *db/db* (Bay, $N = 8$ mice/14 cells; Cilo, $N = 7$ mice/15 cells; Roli, $N = 9$ mice/14 cells) CMs. Representative FRET traces of selective PDE2, PDE3, and PDE4 inhibition post selective β_2-AR stimulation (100 nM ISO in the presence of 100 nM CGP20712A) in (*H–I*) *db/+* (Bay, $N = 6$ mice/13 cells; Cilo, $N = 5$ mice/13 cells; Roli, $N = 8$ mice/12 cells) and (*J–L*) *db/db* (Bay, $N = 8$ mice/16 cells; Cilo, $N = 8$ mice/15 cells; Roli, $N = 8$ mice/15 cells) CMs. (*M–N*) Quantification of FRET responses as % FRET change to IBMX 100 μM. Normal distribution was confirmed by Kolmogorov–Smirnov test ($P > 0.1$) followed by (*M*, *N*) analysis by nested ANOVA. *$P < 0.05$ vs. *db/+* same condition.

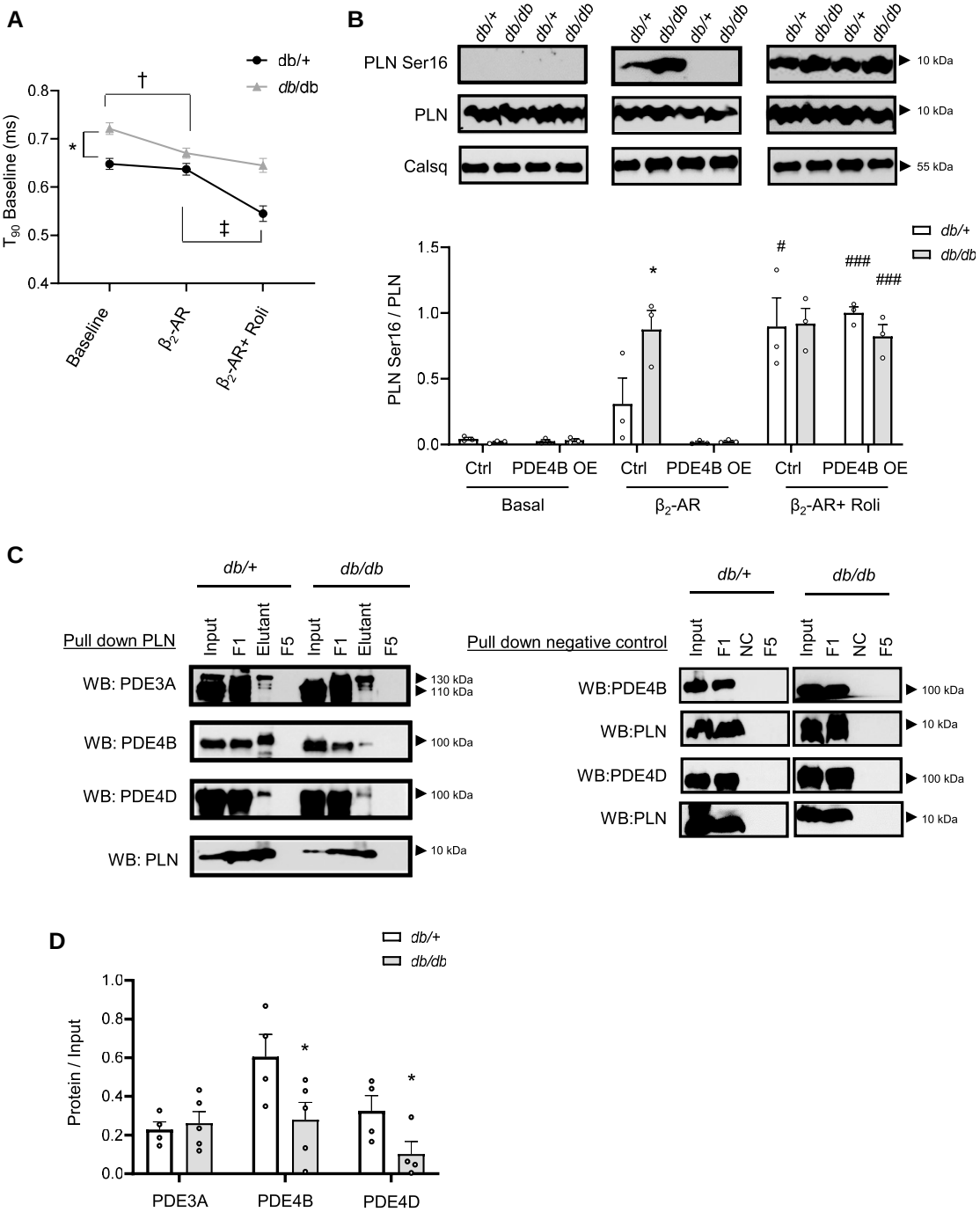

Figure 4 Loss of PDE4 association with PLN. (*A*) Quantification of T_{90} calcium reuptake with 10 μM Roli treatment post selective β_2-AR stimulation (70 nM ISO + 100 nM CGP20712A) in *db/+* ($N = 3$ mice/38 cells) and *db/db* ($N = 3$ mice/40 cells) CMs. Representative fluorescence traces are shown in Supplementary material online, *Figure S6D and E*. (*B*) Representative blots and quantification of Ser16 phosphorylated PLN/total PLN in control and PDE4B overexpressing (OE) CMs under basal conditions and post selective β_2-AR stimulation (100 nM ISO + 100 nM CGP20712A) without 10 μM Roli ($N = 3$ mice/group). pPLN and total PLN intensities were first normalized on Calsq before calculating the pPLN/PLN ratio. (*C*) Co-IP performed with PLN pull down, representative blots for PDE3A, PDE4B, and PDE4D (F1 being the first flow through when beads washed, F5 the final flow through when beads washed, and Elutant, the eluted protein samples bound to the beads). The right-hand side shows negative controls performed under the same conditions using an unrelated antibody for IP. (*D*) Quantification of Co-IP normalized to input ($N = 5$ mice/group). Normal distribution was confirmed by Kolmogorov–Smirnov test ($P > 0.1$) in all data except in (*C*) where β_2-AR *db/+*, $P = 0.0777$ and β_2-AR + Roli *db/db*, $P = 0.0016$. Normally distributed data in (*B* and *D*) analysed mixed ANOVA followed by Wald χ^2 test and Sidak multiple comparisons test. Data not normally distributed in (*C*) analysed by mixed ANOVA followed by Kruskal–Wallis test and Dunn's multiple comparisons test. *$P < 0.05$ vs. *db/+* same condition; #$P < 0.05$ and ###$P < 0.001$ vs. β_2-AR stimulation same group; †$P < 0.05$ in *db/+* compared to *db/+* at basal; and ‡$P < 0.05$ in *db/+* compared to *db/+* post β_2-AR stimulation.

between the groups (see Supplementary material online, *Figure S6F*), suggesting reduced PDE4-specific effect on calcium re-uptake in *db/db* cells. Furthermore, in *db/+* CMs, selective β_2-AR stimulation increased PLN Ser16 phosphorylation in the presence of Roli (while as mentioned, in the absence of PDE4 inhibition, β_2-AR stimulation fails to increase Ser16 phosphorylation in *db/+* CMs), while in *db/db* CMs, Roli treatment did not provide an additive effect to β_2-AR-stimulated Ser16 phosphorylation (*Figure 4B*). Therefore, these results suggest there is a reduced coupling between the β_2-AR-regulated SERCA2a microdomain with PDE4 in *db/db* CMs, which may mediate the increased β_2-AR-induced cAMP amplitudes and lusitropic effects.

To confirm this hypothesis, Co-IP experiments were performed in which PLN was pulled down and its direct association with PDEs was assessed. While previously documented PDE3A association with PLN/SERCA complex[21] was unchanged between *db/+* and *db/db* hearts, reduced association with both PDE4B and PDE4D, only the latter being previously reported in the literature,[22] was observed in *db/db* heart lysates compared to that in *db/+* heart lysates (*Figure 4C* and *D*), which correlated with reduced PDE4 activity in these co-immunoprecipitates (see Supplementary material online, *Figure S9A*), thereby confirming a reduced association of PDE4 within the PLN/SERCA2a microdomain in *db/db* mice. Supporting this, a reduced expression of *AKAP7*, which is known to tether PDE4D to the PLN microdomain,[23] was also observed in *db/db* CMs using NanoString nCounter analysis at the mRNA level (see Supplementary material online, *Figure S3C*) without major alterations of adenylyl cyclase mRNAs (see Supplementary material online, *Figure S3D–H*) or protein expression of PKA regulatory RIIα subunit (see Supplementary material online, *Figure S3I* and *K*). Indeed, we could also detect a reduced association between AKAP7 and PLN in *db/db* hearts using Co-IP (see Supplementary material online, *Figure S9B*). Subcellular fractionation analysis performed using sucrose density gradients showed that PDE4B and PDE4D indeed co-localize with PLN in SR fractions (see Supplementary material online, *Figure S9D* and *E*). Here and in all other immunoblots, we could detect only one long PDE4B isoform, which can be identified as PDE4B3 according to its size, whereas PDE4D3, 5, 7, and 8 isoforms were expressed in both *db/+* and *db/db* by reverse transcriptase (RT)–PCR analysis (see Supplementary material online, *Figure S3L*), as previously documented.[24–26]

3.5 Overexpression of PDE4B diminishes β_2-AR-induced cAMP production within the PLN/SERCA2a microdomain in *db/db* CMs

To further elucidate whether the loss of PDE4 is responsible for the β_2-AR cAMP pools within the PLN microdomain in *db/db* CMs, we aimed to determine whether a restoration of PDE4 could normalize β_2-AR signalling by adenoviral gene transfer of PDE4B3. First, we assessed the degree of PDE4 overexpression, which was increased by six- to eight-fold at the protein and three- to five-fold at the enzymatic activity level (see Supplementary material online, *Figure S10*). We also confirmed that PDE4B overexpression was accompanied by a complete abolishment of β_2-AR-induced PLN Ser16 phosphorylation in these cells (*Figure 4B*), while Roli treatment restored PLN Ser16 phosphorylation levels in *db/db* CMs overexpressing PDE4B3 to that of control *db/db* levels (*Figure 4B*). Next, we performed FRET measurements to assess β_2-AR/cAMP responses. Indeed, PDE4B overexpression in *db/db* CMs resulted in a blunted increase in FRET amplitudes post selective β_2-AR stimulation (4% vs. 40% of max, respectively; see Supplementary material online, *Figure S10*). Together, these data support the hypothesis that the loss of PDE4 coupling with the PLN/SERCA2a microdomain drives increased β_2-AR control of local cAMP dynamics and alterations of calcium cycling.

To further corroborate these findings, we overexpressed PDE4B3 using adeno-associated virus *in vivo* under the control of a CM-specific troponin T promoter. We could detect an approximately five-fold PDE4B overexpression without compensatory changes in PDE2A or PDE3A expression in CMs isolated from these mice and a completely blunted β_2-AR-induced PLN Ser16 phosphorylation (see Supplementary material online, *Figure S11*). At the functional level, we could not see any significant effect of PDE4B3 overexpression on the already relatively severe HFpEF phenotype in the *db/db* mice (*Table 2*). Interestingly, PDE4B overexpression in

Table 2 Effect of *in vivo* CM-specific PDE4B overexpression on basic echocardiography parameters

Variable	*db/+* LUC	*db/+* PDE4B	*db/db* LUC	*db/db* PDE4B
Weight (g)	31.8 ± 11.0	29.9 ± 3.7	53.5 ± 5.2	52.9 ± 10.0
Heart rate (b.p.m.)	415 ± 61	466 ± 27	413 ± 26	456 ± 57
IVSd (mm)	0.84 ± 0.13	0.91 ± 0.07	0.86 ± 0.10	0.89 ± 0.12
IVSs (mm)	1.32 ± 0.29	1.24 ± 0.11	1.31 ± 0.20	1.27 ± 0.20
LVIDd (mm)	4.14 ± 0.23	4.38 ± 0.26	4.15 ± 0.31	3.99 ± 0.48
LVIDs (mm)	2.96 ± 0.62	3.62 ± 0.28	2.89 ± 0.31	2.98 ± 0.64
LVPWd (mm)	0.64 ± 0.13	0.69 ± 0.10	0.83 ± 0.09**	0.81 ± 0.09**
LVPWs (mm)	1.00 ± 0.45	0.87 ± 0.09	1.16 ± 0.18	1.01 ± 0.17
Estimated LV mass (mg)	119.3 ± 16.1	145.1 ± 20.0*	131.6 ± 23.6	129.1 ± 19.0
LA (mm)	0.96 ± 0.06	1.21 ± 0.11**	1.28 ± 0.18**	1.19 ± 0.15*
EF (%)	53.3 ± 18.4	36.5 ± 4.9*	57.4 ± 10.6	49.2 ± 16.5
FS (%)	28.8 ± 14.2	17.4 ± 2.6	30.2 ± 7.4	25.5 ± 11.3
Peak E-wave	663 ± 98	714 ± 82	685 ± 151	525 ± 150
Peak A-wave	424 ± 77	446 ± 105	345 ± 114	260 ± 121
E/A	1.25 ± 0.12	0.82 ± 0.09**	1.37 ± 0.60	N/A
IVRT (ms)	17.8 ± 1.9	15.1 ± 1.3	16.4 ± 1.2	16.9 ± 1.7
e′	25.53 ± 6.14	19.40 ± 4.68	14.20 ± 8.98	11.22 ± 5.36
E/e′	31.12 ± 11.90	37.95 ± 6.83	65.57 ± 33.30*	51.99 ± 19.68*

Mice were i.v. injected into tail vein with 1×10^{12} viral genomes of PDE4B or luciferase (LUC, control) at the age of 6 weeks. Echocardiography was performed at 16 weeks of age. Data presented as mean ± SD. Normal distribution was confirmed by Kolmogorov–Smirnov test ($P > 0.1$) in all parameters, which were analysed by unpaired *t*-test ($N = 7$ mice/group).
Abbreviations as in *Table 1*.
*$P < 0.05$ and **$P < 0.01$ compared to *db/+ LUC* controls.

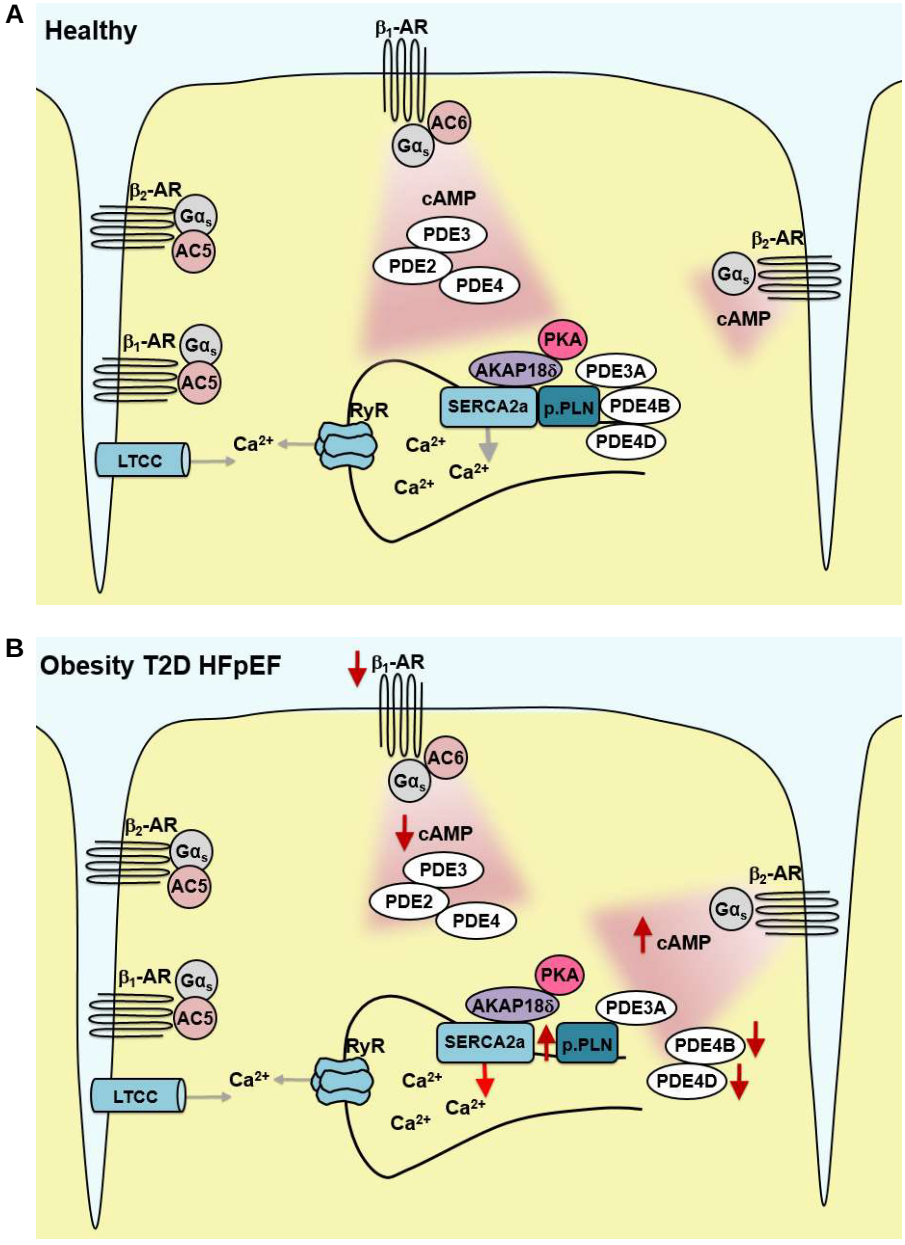

Figure 5 Summary diagrams of cAMP dynamics within the SERCA2a microdomain. In (*A*) healthy *db/+* CMs, cAMP pools are generated by β_1-AR signalling with PDE4B and PDE4D associating with PLN and locally controlling β_2-AR/cAMP effects in this microdomain. In (*B*) *db/db* CMs, β_1-AR-induced cAMP pools and PLN phosphorylation are desensitized and β_2-AR signalling is enhanced, due to a loss of PDE4 coupling with the β_2-AR and association with PLN.

healthy *db/+* mice led to a significant increase in LA size, indicating early signs of diastolic dysfunction and increased LA filling pressures, suggesting that β_2-AR/cAMP regulation of the SERCA2a microdomain might be needed for proper cardiac relaxation and protection from HFpEF.

4. Discussion

In summary, we have uncovered disease-specific alterations of cAMP dynamics within the PLN/SERCA2a microdomain that provide insights into the mechanisms of altered PLN/SERCA2a activity in HFpEF caused by obesity and T2D. The major findings from the study are summarized in *Figure 5A* and *B* and include the following: (i) a desensitization of β_1-AR induced cAMP pools within the PLN/SERCA2a microdomain and of calcium re-uptake into the SR in *db/db* CMs; (ii) *db/db* CMs exhibit a pronounced β_2-AR control of cAMP pools and PLN/SERCA2a activity that is not detected in healthy *db/+* CMs; and (iii) this altered β-AR subtype control of the PLN/SERCA2a microdomain allows for β_2-AR-induced PLN phosphorylation and enhanced CM relaxation and appears to be driven by a loss of PDE4 coupling with the microdomain.

Considering the suitability of obesity and T2D HFpEF mouse model chosen, there is no question that in this field, we face considerable challenges in the identification of a 'true' obesity and T2D HFpEF model.[27,28] These difficulties stem from the reality of the clinical manifestation of HFpEF in which patients present with multiple co-morbidities (including obesity, T2D, hypertension, and chronic obstructive pulmonary disease) as well

as the inconsistent diagnosis criteria of HFpEF that ultimately rely partly on the presence of subjective symptoms described by the patient in order to distinguish between the presence of diastolic dysfunction vs. HFpEF. As such, we chose an obese and T2D mouse model most representative of human obesity and T2D, in which there is an early presence of insulin resistance that drives the development of T2D that is not complicated by the presence of a high-fat diet and that does not skip the essential pathological stage of insulin resistance. While the phenotype is promoted by a defective leptin receptor, leptin resistance is widely reported in both obesity and T2D,[29,30] albeit likely at a less severe degree to that in the $lepr^{db}$ mice. Importantly, at the time point studied, the mice presented with overtly increased LA filling pressures, the main characteristic of HFpEF[31] that was accompanied by the presence of fibrosis, indicative of LV stiffening, another hallmark of HFpEF.[32]

The remodelling events identified in the PLN/SERCA2a microdomain differ from that which we have previously observed in a mouse model of cardiac hypertrophy and early heart failure induced by transverse aortic constriction (TAC). In this TAC model of early HFrEF, we uncovered a loss of β_1-AR-induced cAMP pools within the PLN/SERCA2a microdomain with no change in the lack of β_2-AR-simulated cAMP levels.[9] This is in contrast to what we have observed in obesity/T2D HFpEF, where a loss of β_1-AR control of cAMP levels was accompanied by a potentially compensatory novel role of the β_2-AR to induce substantial increases in cAMP pools within the PLN/SERCA2a microdomain. These differences between the studies can be resolved by assessing PDE coupling, where in our TAC model (in which cAMP levels remained exclusively stimulated by the β_1-AR) we identified post ISO stimulation the presence of increased PDE2 control of cAMP pools within the PLN/SERCA2a microdomain, which partially explains the blunted ISO-induced cAMP responses observed. However, in the *db/db* CMs, we observed no change in FRET responses with inhibition of PDE2, PDE3, or PDE4 post selective β_1-AR stimulation, but a reduction in *Ardb1* gene expression, suggesting that the desensitization of β_1-AR-stimulated cAMP pools within the PLN/SERCA2a microdomain is not mediated via alterations in the downstream regulation of cAMP but rather a direct decrease in β_1-AR expression. Indeed, this hypothesis is consistent with the observation that this desensitization is present at submaximal β_1-AR stimulation but not at saturating levels that may mask differences in β_1-AR expression levels. Again, in contrast to our TAC model, we identified a decreased cAMP response with PDE4 inhibition post selective β_2-AR stimulation. Thus, this PDE can mediate the increased cAMP responses post selective β_2-AR stimulation. Furthermore, another striking difference between the two disease states, while in our TAC model we observed a decreased basal PDE4 control of cAMP, in the current study, *db/db* CMs exhibited an increased basal PDE4 activity. Therefore, considering these results, it is tempting to speculate that this new role for the β_2-AR to regulate PLN/SERCA2a cAMP levels as well as the increased basal PDE4 activity in *db/db* CMs may be compensatory mechanisms to prevent prolonged cardiac relaxation upon β-AR stimulation and to protect against hyperphosphorylation of PLN under basal conditions. Indeed, while basal calcium re-uptake into the SR was prolonged in *db/db* CMs, upon selective β_2-AR stimulation, we observed an accelerated calcium re-uptake that could not be induced in healthy *db/+* CMs. Furthermore, no changes in basal PLN phosphorylation between the *db/+* and *db/db* CMs were detected supporting the presence of inhibition of basal cAMP pools within the PLN/SERCA2a microdomain in a setting that characteristically exhibits enhanced sympathetic drive.[33]

While PDE4D has previously been shown to associate with PLN/SERCA2a and to regulate basal cAMP levels within the PLN/SERCA2a microdomain,[22] in the current study, we detected an association with not only PDE4D but also PDE4B in *db/+* CMs, with a pronounced reduction in both PDE4B and PDE4D association in *db/db* CMs. This association with PDE4B is somewhat unexpected considering past findings, in which PDE4B is reported to associate with $Ca_V1.2$ of the LTCC.[34] However, $Pde4^{-/-}$ mice have been shown to exhibit altered calcium transients. For example, CMs from $Pde4b^{-/-}$ mice exhibited a trend for accelerated SR calcium re-uptake (while this was significantly accelerated in $Pde4b^{-/-}$ mice), and both $Pde4b^{-/-}$ and $Pde4d^{-/-}$ CMs exhibited increased spontaneous calcium release, supporting not only a role for PDE4D but also PDE4B in the regulation of SR calcium transients within the PLN/SERCA2a microdomain.[35] Furthermore, as PDE4B and PDE4D protein expression remained unchanged in whole cell lysates, the loss of PDE4B and PDE4D appears to be microdomain specific. Interestingly, we also observed reduced expression of AKAP7, which has previously been shown to tether PDE4D to PLN,[23] with the amount of AKAP7 pulled down together with PLN being also reduced in our study, further supporting the presence of alterations in PDE4 localization at the microdomain level.

Overexpression of PDE4B3 *in vitro* or *in vivo* could blunt β_2-AR-induced cAMP signals in the SERCA2a microdomain and the downstream PLN phosphorylation. While PDE4B3 overexpression using serotype 9 adeno-associated virus and cytomegalovirus promoter, similar to beta-blockers, is cardioprotective in various models of HFrEF including pressure-overload induced heart failure,[35] we could not see any significant effect of CM-specific PDE4B3 overexpression in our HFpEF model and even an increase in atria size when injected into *db/+* mice. This highlights a protective effect of the local loss of this PDE from the SERCA2a microdomain in terms of cardiac relaxation and diastolic function. Also, this is compatible with the notion that HFpEF is not responsive to traditional beta-blocker therapy and calls for new specific therapies that should be different from those used for systolic heart failure.

In summary, we present data in which we have generated a novel mouse model that has allowed us, for the first time, to assess cAMP dynamics at the microdomain level in HFpEF caused by obesity and T2D. We have uncovered disease-specific remodelling events with the PLN/SERCA2a microdomain that provided key insights into the mechanisms of dysregulated PLN/SERCA2a activity in obesity and T2D HFpEF that stem from altered β-AR subtype control and PDE coupling.

Supplementary material

Supplementary material is available at *Cardiovascular Research* online.

Authors' contributions

Study concept and design: K.A.D.J. and V.O.N.; performed experiments: P.L., K.A.D.J., S.S.H., H.S., and V.O.N.; data analysis and interpretation: P.L., K.A.D.J., H.S., R.W., P.R., O.J.M., and V.O.N.; wrote the manuscript: K.A.D.J. and V.O.N. All authors edited and approved the final manuscript.

Conflict of interest: none declared.

Funding

The work was funded by the Gertaud und Heinz-Rose Foundation grant to K.A.D.J. and V.O.N. and Chinese Government Scholarship to P.L.

Data availability

The data underlying this article are available within the article and in its online supplementary material.

References

1. Tsujimoto T, Kajio H. Beta-blocker use and cardiovascular event risk in patients with heart failure with preserved ejection fraction. *Sci Rep* 2018;**8**:9556.
2. Savji N, Meijers WC, Bartz TM, Bhambhani V, Cushman M, Nayor M, Kizer JR, Sarma A, Blaha MJ, Gansevoort RT, Gardin JM, Hillege HL, Ji F, Kop WJ, Lau ES, Lee DS, Sadreyev R, van Gilst WH, Wang TJ, Zanni MV, Vasan RS, Allen NB, Psaty BM, van der Harst P, Levy D, Larson M, Shah SJ, de Boer RA, Gottdiener JS, Ho JE. The association of obesity and cardiometabolic traits with incident HFpEF and HFrEF. *JACC Heart Fail* 2018;**6**:701–709.
3. MacDonald MR, Petrie MC, Varyani F, Ostergren J, Michelson EL, Young JB, Solomon SD, Granger CB, Swedberg K, Yusuf S, Pfeffer MA, McMurray JJ, Investigators C. Impact of diabetes on outcomes in patients with low and preserved ejection fraction heart failure: an analysis of the Candesartan in Heart failure: Assessment of Reduction in Mortality and morbidity (CHARM) programme. *Eur Heart J* 2008;**29**:1377–1385.
4. De Jong KA, Czeczor JK, Sithara S, McEwen K, Lopaschuk GD, Appelbe A, Cukier K, Kotowicz M, McGee SL. Obesity and type 2 diabetes have additive effects on left ventricular remodelling in normotensive patients-a cross sectional study. *Cardiovasc Diabetol* 2017;**16**:21.

5. Khan MAB, Hashim MJ, King JK, Govender RD, Mustafa H, Al Kaabi J. Epidemiology of type 2 diabetes—global burden of disease and forecasted trends. *J Epidemiol Glob Health* 2020;**10**: 107–111.
6. Conti M, Beavo J. Biochemistry and physiology of cyclic nucleotide phosphodiesterases: essential components in cyclic nucleotide signaling. *Annu Rev Biochem* 2007;**76**:481–511.
7. Bers DM. Cardiac excitation-contraction coupling. *Nature* 2002;**415**:198–205.
8. Perera RK, Nikolaev VO. Compartmentation of cAMP signalling in cardiomyocytes in health and disease. *Acta Physiol* 2013;**207**:650–662.
9. Sprenger JU, Perera RK, Steinbrecher JH, Lehnart SE, Maier LS, Hasenfuss G, Nikolaev VO. In vivo model with targeted cAMP biosensor reveals changes in receptor-microdomain communication in cardiac disease. *Nat Commun* 2015;**6**:6965.
10. Perera RK, Sprenger JU, Steinbrecher JH, Hübscher D, Lehnart SE, Abesser M, Schuh K, El-Armouche A, Nikolaev VO. Microdomain switch of cGMP-regulated phosphodiesterases leads to ANP-induced augmentation of β-adrenoceptor-stimulated contractility in early cardiac hypertrophy. *Circ Res* 2015;**116**:1304–1311.
11. Berisha F, Gotz KR, Wegener JW, Brandenburg S, Subramanian H, Molina CE, Ruffer A, Petersen J, Bernhardt A, Girdauskas E, Jungen C, Pape U, Kraft AE, Warnke S, Lindner D, Westermann D, Blankenberg S, Meyer C, Hasenfuss G, Lehnart SE, Nikolaev VO. cAMP imaging at ryanodine receptors reveals β_2-adrenoceptor driven arrhythmias. *Circ Res* 2021; **129**:81–94.
12. De Jong KA, Nikolaev VO. Multifaceted remodelling of cAMP microdomains driven by different aetiologies of heart failure. *FEBS J* 2021;**288**:6603–6622.
13. Sakata S, Lebeche D, Sakata Y, Sakata N, Chemaly ER, Liang LF, Padmanabhan P, Konishi N, Takaki M, del Monte F, Hajjar RJ. Mechanical and metabolic rescue in a type II diabetes model of cardiomyopathy by targeted gene transfer. *Mol Ther* 2006;**13**:987–996.
14. Vasanji Z, Cantor EJ, Juric D, Moyen M, Netticadan T. Alterations in cardiac contractile performance and sarcoplasmic reticulum function in sucrose-fed rats is associated with insulin resistance. *Am J Physiol Cell Physiol* 2006;**291**:C772–C780.
15. Fredersdorf S, Thumann C, Zimmermann WH, Vetter R, Graf T, Luchner A, Riegger GA, Schunkert H, Eschenhagen T, Weil J. Increased myocardial SERCA expression in early type 2 diabetes mellitus is insulin dependent: in vivo and in vitro data. *Cardiovasc Diabetol* 2012;**11**:57.
16. Belke DD, Swanson EA, Dillmann WH. Decreased sarcoplasmic reticulum activity and contractility in diabetic *db*/*db* mouse heart. *Diabetes* 2004;**53**:3201–3208.
17. Frederich RC, Hamann A, Anderson S, Lollmann B, Lowell BB, Flier JS. Leptin levels reflect body lipid content in mice: evidence for diet-induced resistance to leptin action. *Nat Med* 1995;**1**:1311–1314.
18. Wang B, Chandrasekera PC, Pippin JJ. Leptin- and leptin receptor-deficient rodent models: relevance for human type 2 diabetes. *Curr Diabetes Rev* 2014;**10**:131–145.
19. Venardos K, De Jong KA, Elkamie M, Connor T, McGee SL. The PKD inhibitor CID755673 enhances cardiac function in diabetic db/db mice. *PLoS One* 2015;**10**:e0120934.
20. Jungen C, Scherschel K, Flenner F, Jee H, Rajendran P, De Jong KA, Nikolaev V, Meyer C, Ardell JL, Tompkins JD. Increased arrhythmia susceptibility in type 2 diabetic mice related to dysregulation of ventricular sympathetic innervation. *Am J Physiol Heart Circ Physiol* 2019;**317**:H1328–H1341.
21. Skogestad J, Albert I, Hougen K, Lothe GB, Lunde M, Eken OS, Veras I, Huynh NTT, Borstad M, Marshall S, Shen X, Louch WE, Robinson EL, Cleveland JC Jr, Ambardekar AV, Schwisow JA, Jonas E, Calejo AI, Morth JP, Tasken K, Melleby AO, Lunde PK, Sjaastad I, Carlson CR, Aronsen JM. Disruption of phosphodiesterase 3A binding to SERCA2 increases SERCA2 activity and reduces mortality in mice with chronic heart failure. *Circulation* 2023;**147**: 1221–1236.
22. Beca S, Helli PB, Simpson JA, Zhao D, Farman GP, Jones PP, Tian X, Wilson LS, Ahmad F, Chen SRW, Movsesian MA, Manganiello V, Maurice DH, Conti M, Backx PH. Phosphodiesterase 4D regulates baseline sarcoplasmic reticulum Ca^{2+} release and cardiac contractility, independently of L-type Ca^{2+} current. *Circ Res* 2011;**109**:1024–1030.
23. Lygren B, Carlson CR, Santamaria K, Lissandron V, McSorley T, Litzenberg J, Lorenz D, Wiesner B, Rosenthal W, Zaccolo M, Tasken K, Klussmann E. AKAP complex regulates Ca^{2+} re-uptake into heart sarcoplasmic reticulum. *EMBO Rep* 2007;**8**:1061–1067.
24. Kerfant B-G, Zhao D, Lorenzen-Schmidt I, Wilson LS, Cai S, Chen SR, Maurice DH, Backx PH. PI3Kγ is required for PDE4, not PDE3, activity in subcellular microdomains containing the sarcoplasmic reticular calcium ATPase in cardiomyocytes. *Circ Res* 2007;**101**: 400–408.
25. Richter W, Jin S-LC, Conti M. Splice variants of the cyclic nucleotide phosphodiesterase PDE4D are differentially expressed and regulated in rat tissue. *Biochem J* 2005;**388**:803–811.
26. Richter W, Day P, Agrawal R, Bruss MD, Granier S, Wang YL, Rasmussen SG, Horner K, Wang P, Lei T, Patterson AJ, Kobilka B, Conti M. Signaling from β1- and β2-adrenergic receptors is defined by differential interactions with PDE4. *EMBO J* 2008;**27**:384–393.
27. Valero-Munoz M, Backman W, Sam F. Murine models of heart failure with preserved ejection fraction: a "fishing expedition". *JACC Basic Transl Sci* 2017;**2**:770–789.
28. Withaar C, Lam CSP, Schiattarella GG, de Boer RA, Meems LMG. Heart failure with preserved ejection fraction in humans and mice: embracing clinical complexity in mouse models. *Eur Heart J* 2021;**42**:4420–4430.
29. Obradovic M, Sudar-Milovanovic E, Soskic S, Essack M, Arya S, Stewart AJ, Gojobori T, Isenovic ER. Leptin and obesity: role and clinical implication. *Front Endocrinol* 2021;**12**: 585887.
30. Bidulescu A, Dinh PC, Sarwary S, Forsyth E, Luetke MC, King DB, Liu J, Davis SK, Correa A. Associations of leptin and adiponectin with incident type 2 diabetes and interactions among African Americans: the Jackson heart study. *BMC Endocr Disord* 2020;**20**:31.
31. Rossi A, Gheorghiade M, Triposkiadis F, Solomon SD, Pieske B, Butler J. Left atrium in heart failure with preserved ejection fraction: structure, function, and significance. *Circ Heart Fail* 2014;**7**:1042–1049.
32. Zile MR, Baicu CF, Ikonomidis JS, Stroud RE, Nietert PJ, Bradshaw AD, Slater R, Palmer BM, Van Buren P, Meyer M, Redfield MM, Bull DA, Granzier HL, LeWinter MM. Myocardial stiffness in patients with heart failure and a preserved ejection fraction: contributions of collagen and titin. *Circulation* 2015;**131**:1247–1259.
33. Thorp AA, Schlaich MP. Relevance of sympathetic nervous system activation in obesity and metabolic syndrome. *J Diabetes Res* 2015;**2015**:341583.
34. Leroy J, Richter W, Mika D, Castro LR, Abi-Gerges A, Xie M, Scheitrum C, Lefebvre F, Schittl J, Mateo P, Westenbroek R, Catterall WA, Charpentier F, Conti M, Fischmeister R, Vandecasteele G. Phosphodiesterase 4B in the cardiac L-type Ca^{2+} channel complex regulates Ca^{2+} current and protects against ventricular arrhythmias in mice. *J Clin Invest* 2011; **121**:2651–2661.
35. Karam S, Margaria JP, Bourcier A, Mika D, Varin A, Bedioune I, Lindner M, Bouadjel K, Dessillons M, Gaudin F, Lefebvre F, Mateo P, Lechene P, Gomez S, Domergue V, Robert P, Coquard C, Algalarrondo V, Samuel J-L, Michel J-B, Charpentier F, Ghigo A, Hirsch E, Fischmeister R, Leroy J, Vandecasteele G. Cardiac overexpression of PDE4B blunts β-adrenergic response and maladaptive remodeling in heart failure. *Circulation* 2020;**142**: 161–174.